This is a preprint, the final version is subject to change, of the American Mineralogist (MSA)
Cite as Authors (Year) Title. American Mineralogist, in press.
DOI: https://doi.org/10.2138/am-2018-6478

Revision 1

Fe-kaolinite in granite saprolite beneath sedimentary kaolin deposits: a mode of Fe substitution for Al in kaolinite

MAYUMI JIGE[1], TETSUICHI TAKAGI[2,*], YOSHIO TAKAHASHI[3], MINAKO KURISU[3], YUKI TSUNAZAWA[2], KAZUYA MORIMOTO[2], MIHOKO HOSHINO[2], and KATSUHIRO TSUKIMURA[2]

[1] Osaka Ohtani University, Department of Education, 3-11-1 Nishikiori-kita, Tondabayashi, Osaka 584-8540 Japan

[2] Geological Survey of Japan, National Institute of Advanced Industrial Science and Technology (AIST), 1-1-1 Higashi, Tsukuba, Ibaraki 305-8567 Japan

[3] University of Tokyo, Department of Earth and Planetary Science, 7-3-1 Hongo, Bunkyo-ku, Tokyo 113-0033 Japan

ABSTRACT

Fe-kaolinite has been detected in granite saprolite beneath sedimentary kaolin deposits in the Seto district of central Japan. Granite saprolite, which was found underneath sedimentary kaolin deposits formed in fluvial and lacustrine environments, had been subjected to kaolinization. The clay fractions of granite saprolite consist mostly of kaolinite with subordinate micaceous clay, quartz and feldspars. Electron probe microanalysis (EPMA) showed that the kaolinite in clay fractions contained an average 3.30-3.72 wt. % of Fe_2O_3, indicative of Fe-kaolinite. Fe+Si was

inversely proportional to Al in Fe-kaolinite, indicating coupled substitution between Fe+Si and Al. The K_2O contents of Fe-kaolinite increased with increasing Fe_2O_3 up to 0.77 wt. %, whereas K did not correlate with other elements, suggesting that K was not contained with the structure of kaolinite but was present in its interlayers. X-ray absorption near-edge structure (XANES) spectroscopy showed that about 60 to 70 % of Fe in the clay fractions is ferric iron, and extended X-ray absorption fine structure (EXAFS) spectroscopy indicated that Fe is situated in octahedral sites replacing Al. Fe-kaolinite was likely precipitated by the infiltration of acidic groundwater with higher Fe and alkali contents into granite saprolite, accompanied by the intense kaolinization of sedimentary kaolin deposits.

Key Words- kaolinite, coupled substitution, granite saprolite, ferric iron, EPMA, EXAFS, XANES, Japan

* E-mail address of corresponding author:
takagi-t@aist.go.jp

INTRODUCTION

Kaolin is a robust clay mineral with a simple chemical composition, $Si_2Al_2O_5(OH)_4$, and is the final weathering product of felsic rocks in temperate regions. Kaolin often contains detectable amount of Fe and Ti (Murray and Lyons 1959). Because Fe and Ti may cause undesired coloring of porcelain products made of kaolin clay, methods have been developed for removal of these

elements from kaolin (e.g., Maynard et al. 1968; Gonzalez and Ruiz 2006). Several studies have described the occurrence and mineralogy of Fe-bearing kaolin, in particular Fe-enriched lateritic soils (e.g., Herbillon et al. 1976; Mendelovici et al. 1979; Tardy and Nahon 1985; Hart et al. 2002). A summary of the impediments in studies of Fe substitution within the structure of kaolinite found that the major issue was distinguishing Fe in kaolinite from other potential Fe-phases, such as oxides, hydroxides, silicates and sulfides (Schroeder and Pruett 1996). These Fe-phases may be present as submicron-sized particles within kaolin clays. Methods used to study Fe-bearing kaolin include electron probe microanalysis (EPMA), electron paramagnetic resonance (EPR) spectrometry (e.g., Balan et al. 1999) and infrared spectrometry (e.g., Delineau et al. 1994).

Fe-bearing kaolin (Fe-kaolinite) has been detected in granite saprolite beneath sedimentary kaolin deposits in the Seto district of central Japan. This Fe-bearing kaolin was found to have specific features, including its complexing with micaceous clay and its participation in the coupled substitution of Fe+Si for Al. This study describes the occurrence in the field of Fe-bearing kaolin, and its mineralogy using X-ray powder diffraction (XRD), EPMA, scanning electron microscopy (SEM), and X-ray absorption fine structure (XAFS) spectroscopy. The substitution of Fe within kaolinite structure was identified, despite some of this Fe being incorporated into micaceous clay.

GEOLOGICAL BACKGROUND

The Seto district

The Seto district of central Japan is in the southern half of the Seto-Tono kaolin field, the largest sedimentary kaolin field in the Japan Arc (Fig. 1). The formations containing kaolin deposits (lower Seto Group) consist of fluvial and lacustrine sediments of late Miocene to Pliocene (Nagasawa 1978). These formations occur as small-scale sedimentary basins 1 to 10 km^2 in size, with several sedimentary basins closely distributed in a 10 x 10 km area. The lower Seto Group unconformably overlies late Cretaceous granitic rocks, and is conformably overlain by thick coarse sediments (upper Seto Group) (Nakayama 1991).

Kaolin clay deposits. Most of the kaolin deposits originated from arkose sandstone beds up to 10 m thick, with most of the feldspars and micas in the sandstones kaolinized in situ. The present mineral assemblage is kaolin clay + quartz, a type of kaolin clay called “gaerome clay” by local miners. Thin ligneous kaolin clay layers up to 2 m thick are frequently embedded within gaerome clay beds, a type of kaolin clay called “kibushi clay”.

Granite saprolite. Unconsolidated weathering crusts of granite basements beneath sedimentary kaolin deposits are widely distributed in the Seto district. Most of these weathering crusts are greenish gray to dark green in color; those have tentatively been named “green saprolite” (Fig. 2a). Although green saprolite appears to be unsorted and viscous sandstone, the original granitic texture may be present (Fig. 2b). The uppermost portions were partly reworked by surface water and contain fragments of rock and pegmatitic mineral in places. Exploration

drilling in the Seto district revealed that the thickness of green saprolite varies from 3 to 24 m.

Limonite crusts. Limonite crusts occur sporadically as layers up to 30 cm thick along the unconformity planes between gaerome clay deposits and green saprolite. Limonite crusts are hard and fragile materials, reddish brown in color, and consist of chert pebbles concreted by fine-grained goethite. The limonite crusts can be regarded as part of the basal conglomerate of the lower Seto group, with iron oxides concreting the interstices of the pebbles.

PROPERTIES OF GREEN SAPROLITE

The rock facies of green saprolite in the Seto district are similar to each other, whereas their colors vary by location. These colors can include greenish gray, dark green, yellowish green and reddish brown, with color variations due to the degree of surface oxidation. Shallower portions of green saprolite were locally bleached by kaolinization in the upper horizons.

Constituent minerals. Green saprolite consists of medium- to coarse-grained quartz, feldspars and lesser amounts of biotite and clays. Clay can constitute up to 38 wt. % of green saprolite (Table 1), a distinguishing feature of the latter. As described below, the clay fraction consists mostly of kaolin clays with subordinate micas.

Whole-rock chemical compositions. Whole-rock chemical compositions of green saprolite were analyzed by X-ray fluorescence spectrometry using the RIGAKU ZSX Primus III+ at the Geological Survey of Japan (GSJ), with analysis performed by the glass bead method (Morita et

al. 2012). The loss on ignition (LOI) of the samples was measured by the gravimetric method through ignition at 900 °C.

The source rocks of green saprolite in the Seto district are late Cretaceous Naegi-Agematsu granites (Makimoto et al. 2004), consisting of coarse- to medium-grained leucocratic biotite granite. The whole-rock chemical compositions of green saprolite were compared with those of the source granites (Ishihara and Murakami 2006). In the diagram of Si-Al-(Ca+Na+K) molar ratios (Fig. 3), green saprolite showed compositions intermediate between gaerome clay and the source granites due to the decrease in green saprolite of alkaline elements. In the diagram of Si-Al-(Fe+Mg) molar ratios, however, the compositions of green saprolite almost overlapped with those of the source granites.

MINERALOGY OF CLAY FRACTIONS

Preparation of clay fractions

Because Fe-kaolinite is present in clay fractions of green saprolite, three representative green saprolite samples present in the Marufuji mine in the central Seto district were selected. Samples M01 and M07 are representative facies of green saprolite taken at depths of 1 and 3 m from the unconformity plane, respectively; and sample M08 was taken from a stockyard of the mine. To investigate the effects of depth on ferric/ferrous ratios, samples M01a, b, c, and d, at depths of 2, 3, 4, and 5 m, respectively were also collected near sample M01.

The green saprolite samples were separated by grain sizes using elutriation and sieving, with

grains under 250 μm in diameter recovered as clay fractions, because the grain size distribution of green saprolite is bimodal with the minimum 53-150 or 150-250 μm. The separated clay fractions were concentrated by centrifugation and dried at 75 °C in a drying oven for 12 hours. The weight percentage of clay fractions ranged from 19 to 38 for seven green saprolite samples (Table 1). The greenish gray color of the clay fractions was maintained during drying. Two representative clay fractions from green saprolite samples M01 and M07 were selected.

Chemical compositions of whole clay fractions

The chemical compositions of the clay fractions were analyzed using the same method used to analyze green saprolite (Table 1). The FeO contents of clay fractions were analyzed spectrophotometrically using 1.10 phenanthroline (Nogami 1996), and the Fe_2O_3 contents were determined by subtracting FeO contents from total Fe_2O_3. The Si/Al ratios of the clay fractions suggest that 81 to 91 mol. % of these fractions are kaolin clay. However, the total Fe_2O_3 contents ranged from 1.94 to 4.93 wt. %, twice as high as those of the source Naegi-Agematsu granite. The $Fe_2O_3/(FeO+Fe_2O_3)$ ratios of the clay fractions ranged from 0.34 to 0.78 (mean, 0.60), ratios higher than that of the source granite (0.37, Imai et al. 1995). However, the clay fractions did not contain magnetite or hematite. Depth-dependent changes in ferric/ferrous ratios and colors of the clay fractions could not be detected.

X-ray powder diffraction analysis of clay fractions

Clay fractions were analyzed by X-ray powder diffraction (XRD) spectrometry using

RIGAKU Roterflex RINT2500 at GSJ. The analytical protocol was as follows: graphite monochromatized CuKα radiation (λ=0.15406 nm) at 40 kV and 100 mA in the 2.5–70 (2θ) range with a scanning rate of 0.5 min^{-1}. The XRD patterns of M01 and M07 are shown in Fig. 4.

The constituent minerals of the M01 and M07 are mainly kaolinite and mica, with smaller amounts of quartz and feldspars. Kaolinite is characterized by the intense reflection of (00λ). Although measurement of the kaolinite crystallinity indices (KCIs) of M01 and M07 was attempted, it was difficult to determine Hinckley indices (Hinckley 1963) due to the interference by quartz, feldspar and mica peaks. Using the full width at half the maximum ($FWHM_{001}$) method (Amigó et al. 1987), it was found that the Hinckley indices were 0.35 for M01 and 0.45 for M07, indicating that the kaolinite was disordered. In mica, the basal reflection is somewhat broad and other peaks of mica are not clearly detected. These features suggest that the mica in these samples is not the remnants of granitic biotite but micaceous clay with lower crystallinity. XRD patterns failed to detect chlorite, vermiculite or smectite.

Electron probe microanalysis of clay fractions

Chemical compositions of kaolin clay in M01 and M07 were analyzed using a JEOL JXA-8530F field-emission electron probe micro analyzer (FE-EPMA) at GSJ. The voltage and current of an electron beam were 15 kV and 20 nA, respectively, for back scattered electron images (BSE) and quantitative analysis and 10 kV and 10 nA, respectively, for compositional mapping. The raw data were corrected by the ZAF method. The clay fractions were enclosed in epoxy resin chips and their surfaces were polished under dry conditions.

BSE images. BSE images are shown in Fig. 5. Clays occur as platy or rectangular grains, and are unsorted in sizes that range from 1 to 150 μm in diameter. Aggregate grains several hundred μm long are frequently observed. The shapes of these grains suggest that part of the clays was derived from feldspars.

Chemical compositions of clays. The Si-Al-Fe triangle diagrams (Fig. 6) can distinguish between higher- and lower-K clays by the boundary of 2 wt. % K_2O. In this study, higher- and lower-K clays were tentatively divided into micaceous clay and Fe-kaolinite, respectively. Although the micaceous clay is rich in Fe and K, their compositions vary widely and differ from those of biotite (annite) and illite. The average total Fe_2O_3 and K_2O contents of micaceous clay were 9.36 and 3.56 wt. % (n=8), respectively, in M01, and 14.26 and 4.98 wt. %, respectively (n=28), in M07.

Representative analyses of Fe-kaolinite are shown in Table 2. Kaolinite generally contains small amounts of Fe and K. The average total Fe_2O_3 and K_2O contents were 3.30 and 0.72 wt. % (n=39), respectively, in M01 and 3.72 and 0.77 wt. % (n=77), respectively, in M07. Measurement of the atoms per formula unit (apfu) for each element showed a clear inverse proportion between Fe+Si and Al (Fig.7a), indicating a coupled substitution between Fe+Si and Al. Although K increases with increasing Fe, the correlation was ambiguous and not linear (Fig. 7b). Any clear correlation between K and other elements was not detected, suggesting that K is not substituted into kaolinite structure but occurs as interlayer cations.

Compositional mapping images. The distribution of Fe in Fe-kaolinite is relatively homogeneous, with no Fe-rich particles observed. Small amounts of halite and gypsum were

present in the center or peripheral part of Fe-kaolinite. In some grains, Fe- and K-rich and Al-poor bands of 1 to 2 μm wide were well developed (Fig. 8a,b,c). A BSE image (Fig. 8d) shows these Fe- and K-rich and Al-poor bands as brighter layers intercalated within a kaolinite. These bands consist of micaceous clay. These micaceous clay bands, however, were not likely to be remnants of magmatic biotite, because the modal contents of biotite in the source granite were less than 5 % and the ubiquitous distribution of micaceous clay was not likely. Even if discrete micaceous clay grains were partly derived from magmatic biotite, most micaceous clay bands would be authigenic during kaolinization.

Scanning electron microscopy of clay fractions

Clay shapes were evaluated using a JEOL JSM-6610LV scanning electron microscope (SEM) at GSJ. Representative scanning electron micrographs are shown in Fig. 9. Kaolinite occurs mostly as various sizes of platy flakes and lesser amounts of stacked and petaline-shaped grains. Trace amounts of acicular halloysite were detected in M01. Most micaceous clay is part of kaolinite, with discrete grains being uncommon.

X-ray absorption fine structure spectroscopy

The M01 and M07 clay fractions were subjected to X-ray absorption near-edge structure (XANES) and extended X-ray absorption fine structure (EXAFS) analyses. The spectra were recorded using the beam line BL12C at KEK Photon Factory (Tsukuba, Japan) for M01 and M07, and the beam line BL01B1 at SPring-8 (Sayo, Japan) for M01 (reanalyzed).

XANES analysis. XANES spectra were determined to assess bulk Fe species in powder samples of M01 and M07. Energy calibration for Fe XANES was performed using a pre-edge peak maximum of hematite at 7.111 keV. It is known that energy of pre-edge peak of Fe K-edge XANES increases with the increase of average oxidation state of Fe in the sample (Wilke et al. 2001) as reflected in those of fayalite (Fe_2SiO_4), magnetite (Fe_3O_4), and hematite (Fe_2O_3) (Fig. 10b). The positions of the pre-edge peaks for M01 and M07 were similar to that of magnetite, suggesting that the $Fe_2O_3/(FeO+Fe_2O_3)$ ratios were about 60 to 70 % (Fig. 10b). These results are consistent with the spectrophotometrically determined $Fe_2O_3/(FeO+Fe_2O_3)$ ratios of M01 and M07 clay fractions.

EXAFS analysis. Fe K-edge EXAFS spectra were obtained for powder samples of M01 and M07, and the EXAFS data were simulated using REX2000 software (Rigaku Co. Ltd.) and FEFF 7.02 (Zabinsky et al. 1995). After extracting EXAFS oscillation by the spline smoothing method to obtain $\mu(0)$, the $\chi(k)$ function weighted by k^3 (Fig. 11a) was Fourier transformed (FT) to obtain a radial structure function (RSF) with a k-range of approximately 2.5 to 10.0 $Å^{-1}$ (Fig. 11b). Using the parameter obtained by the FEFF 7.02, the distinct shells of the RSF were back-transformed to k-space for spectral simulation (Fig. 11a). The fitting results are summarized in Table 3.

In assessing M01, XANES spectrum was similar to that of ferrihydrite, suggesting ferrihydrite or ferrihydrite-like materials (Fig. 10a). To verify this result, an M01 sample was treated with a reducing agent ($NH_2OH{\cdot}HCl$) to dissolve Fe-hydroxide (Tessier et al. 1979) and reanalyzed the sample. However, as shown in Fig. 12, the XANES spectra of the treated and

untreated samples were identical, indicating that Fe is not in the state of ferrihydrite or ferrihydrite-like materials. The first neighboring element was likely oxygen, and the Fe-O distance 1.97 Å, indicating that Fe is in octahedral sites (Fig. 11b). The second neighboring elements are Al and Si. The distances between Fe-Al (2.94 Å) and between Fe-Si (3.24 Å) are in good agreement with the local structure of kaolinite (Smrcok et al. 2010), indicating that Fe^{3+} has replaced Al^{3+} in the kaolinite of the M01 sample.

In assessing M07 (Fig. 13), the first neighboring element was likely oxygen, and the Fe-O distance 1.97 Å, indicating that Fe is in octahedral sites. Similar to the results of M01, the second neighboring elements are Al and Si. The distances between Fe-Al (2.95 Å) and between Fe-Si (3.29 Å) are in good agreement with the local structure of kaolinite. Thus, the results also indicate that Fe^{3+} has replaced Al^{3+} in the kaolinite of the M07 sample.

DISCUSSION

A mode of Fe substitution for Al in kaolinite

The EPMA and XAFS analyses showed that the clay fractions of green saprolite contain Fe-kaolinite, even if a fraction of Fe is in micaceous clay. There was no evidence of other Fe-bearing particles, indicating that the greenish gray color of clay fractions is mainly due to Fe-kaolinite. Fe has been detected in gaerome clay in the Seto district, with energy dispersive X-ray spectrometry with a transmission electron microscope finding that the irregularly-shaped platy kaolinite contains 0.9-2.1 wt. % of Fe_2O_3 (Tomura et al. 1981). The Fe contents could not

be reduced by treatment with dilute HCl and H_2O_2, indicating that the Fe in gaerome clay does not result from the surface adhesion of Fe oxides-hydroxides; rather, Fe is present in the crystal structure of kaolinite. Our findings are consistent with the results of the earlier study.

The present study also showed a coupled substitution of Fe+Si for Al in Fe-kaolinite. The stoichiometric calculation of ferric/ferrous ratios in Fe-kaolinite were difficult, because the variation of Fe/Si molar ratios with Al (apfu) were rather scattered. Assuming that Fe in Fe-kaolinite is ferric iron, the end members consist of $Si_2Al_{1.9}(Fe^{3+}_{1.0}Si_{0.1})_{0.09}O_7$ and $Si_2Al_{1.6}(Fe^{3+}_{1.0}Si_{0.4})_{0.27}O_7$, with their chemical compositions varying between them without discontinuity. This chemical variation would represent a type of solid-solution in natural kaolinite. A study of the substitution of octahedral Al^{3+} by Fe^{3+} in kaolinite indicated that the Fe-rich end member of Fe-kaolinite is $Si_2Al_{1.4}Fe_{0.6}O_7$ (Iriarte et al. 2005). Although composition is necessary to determine in cases of isomorphic substitution, the Al apfu values (O=7.0) of Fe-kaolinite in this study were entirely within the ranges for M01 (1.91–1.69) and M07 (1.93–1.53).

Precipitation processes of Fe-kaolinite

Fe-kaolinite in green saprolite was precipitated by the kaolinization of feldspars and micas in weathering crusts of basement granite. The distribution of green saprolite is restricted beneath sedimentary kaolin deposits in the Seto district. Thus, the precipitation of Fe-kaolinite is closely linked with the formation of sedimentary kaolin deposits. Similar to kaolin deposits in Georgia (e.g., Kesler 1956; Kogel et al. 2002), elements such as Fe, Ca, Na and K were leached out by acidic groundwater during the formation of kaolin deposits. The presence of limonite crusts along

unconformity planes suggests that at least some of the acidic groundwater containing the leached elements infiltrated into weathering crusts of basement granite. Fe-kaolinite would be precipitated due to the infiltration of the acidic groundwater with higher Fe and alkali concentrations. A schematic cross section is shown in Fig. 14. As described above, the sedimentary kaolin deposits formed in several small sedimentary basins. The hydraulic system of each sedimentary basin would be almost independent, and acidic groundwater had accumulated in the basin. The formation of green saprolite and Fe-kaolinite is also attributable to the geological situation.

IMPLICATIONS

A clue to explaining the origin of large-scale sedimentary kaolin deposits

It has been thought that large-scale sedimentary kaolin deposits such as those in the central Georgia and Seto districts were formed by intense kaolinization of arkose sediments. However, the assumed process of the kaolinization and leaching out of mafic and alkali elements without hydrothermal activities remains unclear. When we investigate this, kaolin deposits themselves offer little information due to their simple mineral assemblage. However, the green saprolite and limonite crusts occurring as a halo of kaolin deposits may be clues to the origin of large-scale sedimentary kaolin deposits. The results of our study indicate that kaolinization extended over basement granites, and part of leached Fe was precipitated into Fe-kaolinite, micaceous clay, and limonite crusts as mostly ferric iron. The oxidation of Fe under low pH conditions would be a key

296 phenomenon for kaolinization.

297

298 **The use of Fe-kaolinite for ceramic raw materials**

299 As far as the authors know, Fe-kaolinite has never used for ceramic raw materials because of
300 its high contents of Fe and micaceous clay. Fe causes the dark calcination color, and micaceous
301 clay brings about the rougher surface of bisques. However, ceramic industries in the Seto district
302 are currently examining the use of Fe-kaolinite due to the local exhaustion of gaerome clay. The
303 estimated reserve of green saprolite in this district is more than ten million tonnes; Fe-kaolinite is
304 a promising alternative resource. This study suggests that some amount of discrete micaceous
305 clay is removable, but the Fe in Fe-kaolinite is not removable by magnetic separation because Fe
306 is incorporated into the kaolin structure. Although, Fe-kaolinite might be bleached by acid
307 chemical treatment, this method would likely be too expensive. Therefore, the issue of utilizing
308 Fe-kaolinite should mainly be resolved by the development of calcination and glazing techniques.

309

310 **ACKNOWLEDGMENTS**

311 We deeply appreciate Sadahisa Sudo, Yoshiaki Kon, Daisuke Araoka, Buenaventurada C.
312 Segwaben, Chizu Namatame, Kumiko Miyakoshi, Izumi Matsunaga, and Akiko Tokumoto for
313 their technical assistance. We also thank Aichi prefectural association of porcelain industries,
314 Aichi prefectural association of silica sand mining industries, Gifu ceramics material association,
315 Marufuji mine Ltd., and Chubu bureau of economy, trade and industry for their financial and
316 political assistance. This study was supported by Grants-in-Aid for scientific research from the

317 Ministry of Education, Culture, Sports, Science and Technology of Japan (16H04073 and
318 16K12627). This work has been performed with the approval of KEK (Proposal Nos. 2015G664
319 and No. 2016G632) and SPring-8 (Proposal No. 2017A1798).

320

321 **REFERENCES CITED**

322 Amigó, J.M., Bastida, J., Garcia Agramunt, M.J., Sanz, A., and Galván, J. (1987) Crystallinity of
323 Lower Cretaceous kaolinites of Teruel (Spain). Proceedings, 6th Meeting of the European Clay
324 Groups, Euroclay, 87, 74-75.

325

326 Balan, E., Allard, T., Boizot, B., Morin, G., and Muller, J-P. (1999) Structural Fe^{3+} in natural
327 kaolinites: new insights from electron paramagnetic resonance spectra fitting at X and Q-band
328 frequencies. Clays and Clay Minerals, 47, 605-616.

329

330 Delineau, T., Allard, T., Muller, J-P., Barres, O., Yvon, J., and Cases, J-M. (1994) FTIR
331 reflectance vs. EPR studies of structural iron in kaolinites. Clays and Clay Minerals, 42,
332 308-320.

333

334 González, J.A., and Ruiz, M. del C. (2006) Bleaching of kaolins and clays by chlorination of iron
335 and titanium. Applied Clay Science, 33, 219-229.

336

337 Hart, R.D., ST Pierre, T.G., Gilkes, R.J., Mckinley, A.J., Siradz, S., and Balwant Singh (2002)

Iron in soil kaolins from Indonesia and Western Australia. Clay Minerals, 37, 671-685.

Herbillon, A.J., Mestdash, M.M., Vielvoye, L., and Derouane, E.G. (1976) Iron in kaolinite with special reference to kaolinite from tropical soils. Clay Minerals, 11, 201-220.

Hinckley, D.N. (1963) Variability in crystallinity values among the kaolin deposits of the coastal plain of Georgia and South Carolina. Clays and Clay Minerals, 11, 229-235.

Imai, N., Terashima, S., Itoh S., and Ando, A. (1995) 994 compilation values for GSJ reference samples, “Igneous rock series”. Geochemical Journal, 29, 91-95.

Iriarte, I., Petit, S., Huertas, F. J., Fiore, S., Grauby, O., Decarreau, A., and Linares, J. (2005) Synthesis of kaolinite with a high level of Fe^{3+} for Al substitution. Clays and Clay Minerals, 53, 1-10.

Ishihara, S., and Murakami, H. (2006) Fractionated ilmenite-series granites in southwest Japan: Source magma for REE-Sn-W mineralizations. Resource Geology, 56, 245-256.

Kesler, T.L. (1956) Environment and origin of the Cretaceous kaolin deposits of Georgia and South Carolina. Economic Geology, 51, 541-554.

Kogel, J.E., Pickering Jr., S.M., Shelobolina, E., Chowns, T., Yuan, J., and Avant Jr., D.M. (2002) Origin of the Georgia-South Carolina commercial-grade kaolins. Pp. 45-50 in: The Georgia Kaolins, Geology and Utilization. Society for Mining, Metallurgy, and Exploration, Inc. (SME), Colorado.

Makimoto, H., Yamada, N., Mizuno, K., Takada, A., Komazawa, M., and Sudo, S. (2004) Geological Map of Japan 1:200,000 Toyohashi and Irago Misaki. Geological Survey of Japan, AIST.

Maynard, R.N., Millman, N., and Iannicelli, J. (1968) A method for removing titanium dioxide impurities in kaolin. Clays and Clay Minerals, 17, 59-62.

Mendelovici, E., Yariv, S.H., and Villalba, R. (1979) Iron-bearing kaolinite in Venezuelan laterites: I. Infrared spectroscopy and chemical dissolution evidence. Clay Minerals, 14, 323-331.

Morita, S., Takagi, T., Kon, Y., and Araoka, D. (2012) The accuracy and determination limits of rock chemical analysis by X-ray fluorescence spectrometry at Mineral Resources Research Group, Geological Survey of Japan. GSJ Open-file report, No. 624, 36p.

Murray, H.H., and Lyons, S.C. (1959) Further correlations of kaolinite crystallinity with chemical

and physical properties. Clays and Clay Minerals, Proceedings of 8th National Conference, 11-22.

Nagasawa, K. (1978) Kaolin minerals. Pp. 189-219 in: Clays and clay minerals of Japan (T. Sudo and S. Shimoda, editors). Developments in Sedimentology 26, Kodansha-Elsevier.

Nakayama, K. (1991) Depositional processes of the Neogene Seto porcelain clay formation in the northern part of Seto city, central Japan. The Journal of Geological Society of Japan, 97, 945-958. (in Japanese with English abstract)

Nogami, K. (1996) Spectrophotometric determination of FeO content in igneous rock by using 1,10 phenanthroline. Kazan, 41, 275-278. (in Japanese)

Schroeder, P.A., and Pruett, R.J. (1996) Fe ordering in kaolinite: Insights from ^{29}Si and ^{27}Al MAS NMR spectroscopy. American Mineralogist, 81, 26-31.

Smrcok, L., Tunega, D., Ramirez-Cuesta, A.J., and Scholtzová, E. (2010) The combined inelastic neutron scattering and solid state DFT study of hydrogen atoms dynamics in a highly ordered kaolinite. Physics and Chemistry of Minerals, 37, 571-579.

Tardy, Y., and Nahon, D. (1985) Geochemistry of laterites, stability of Al-goethite, Al-hematite,

and Fe^{3+}-kaolinite in bauxite and ferricretes: an approach to the mechanism of concretion formation. American Journal of Science, 285, 865-903.

Tessier, A., Campbell, P.G.C., and Bisson, M. (1979) Sequential extraction procedure for the speciation of particulate trace metals. Analytical Chemistry, 51, 845-851.

Tomura, S., Kitamura, M., Shibasaki, Y., and Maeda, T. (1981) Iron in gairome clay- analytical electron microscope study. Yogyo-Kyokai-Shi, 98, 362-366. (in Japanese with English abstract)

Wilke, M., Farges, F., Petit, P.E., Brown Jr., G.E., and Martin, F. (2001) Oxidation state and coordination of Fe in minerals: An Fe K-XANES spectroscopic study. American Mineralogist, 86, 714-730.

Zabinsky, S.I., Rehr, J.J., Ankudinov, A., Albers, R.C., and Eller, M.J. (1995) Multiple-scattering calculations of X-ray-absorption spectra. Physical Review B 52, 2995-3009.

418 Captions of Figures

419

420 **FIGURE 1.** Geologic map of the Seto district and the surrounding area in central Japan. The map
421 is a simplified version of that reported in Makimoto et al. (2004).

422

423 **FIGURE 2.** (a) An outcrop of gaerome clay, limonite crusts, and green saprolite in the Akatsuki
424 mine, (b) Close-up photograph of green saprolite in the Marufuji mine.

425

426 **FIGURE 3.** Si-Al-(Ca+Na+K) and Si-Al-(Fe+Mg) triangle diagrams, showing the whole-rock
427 chemical compositions of gaerome clay, kibushi clay, green saprolite, and Naegi-Agematsu
428 granite, the source of green saprolite.

429

430 **FIGURE 4.** X-ray powder diffraction patterns of randomly oriented clay fractions in samples (a)
431 M01 and (b) M07. Kln = kaolinite, Mca = mica, Qtz = Quartz, and Fsp = feldspar.

432

433 **FIGURE 5.** Back-scattered electron images of polished chips enclosing clay fractions of (a) M01
434 and (b) M07.

435

436 **FIGURE 6.** Si-Al-Fe triangle diagrams showing the chemical compositions of Fe-kaolinite and
437 micaceous clay within M01 and M07.

438

FIGURE 7. Diagrams showing the relationships between (a) Al and (Fe+Si) and (b) Fe and K in Fe-kaolinite. apfu= atoms per formula unit

FIGURE 8. Elemental mapping images of (a) Fe, (b) K, and (c) Al and a back scattered electron image of Fe-kaolinite in M07.

FIGURE 9. Scanning electron micrographs of Fe-kaolinite in M01 and M07.

FIGURE 10. Fe K-edge XANES spectra (a) and their pre-edge spectra (b) of clay fractions M01 and M07, and of reference Fe model compounds of hematite, ferrihydrite, magnetite, chlorite, and fayalite.

FIGURE 11. (a) Normalized K^3-weighted EXAFS of M01 and (b) its corresponding Fourier Transformed magnitude. Red dots and solid curves represent experimental data and fitting simulations of the experimental data, respectively.

FIGURE 12. Fe K-edge XANES spectra of untreated M01 (solid curve) and of M01 treated with a reducing agent (red curve).

FIGURE 13. (a) Normalized K^3-weighted EXAFS of M07 and (b) its corresponding Fourier Transformed magnitude.

This is a preprint, the final version is subject to change, of the American Mineralogist (MSA)
Cite as Authors (Year) Title. American Mineralogist, in press.
DOI: https://doi.org/10.2138/am-2018-6478

460

461 **FIGURE 14.** Schematic cross section showing the precipitation processes of Fe-kaolinite in the

462 Seto district.

463

This is a preprint, the final version is subject to change, of the American Mineralogist (MSA)
Cite as Authors (Year) Title. American Mineralogist, in press.
DOI: https://doi.org/10.2138/am-2018-6478

Table 1 Chemical compositions of clay fractions in green saprolite

Sample	M01	M07	M08	M01a	M01b	M01c	M01d
SiO_2 (wt.%)	51.58	49.59	49.10	48.15	50.93	50.21	51.02
TiO_2	0.63	0.55	0.76	0.97	0.45	0.48	0.45
Al_2O_3	29.92	29.45	32.92	34.12	30.99	30.83	30.24
Fe_2O_3	2.29	3.70	2.04	0.67	0.83	2.49	2.19
FeO	1.11	1.11	0.56	1.14	1.64	1.14	1.53
MnO	0.05	0.06	0.03	0.02	0.02	0.04	0.05
MgO	0.51	0.66	0.37	0.26	0.30	0.46	0.52
CaO	0.16	0.45	0.15	0.18	0.16	0.70	0.58
Na_2O	0.23	0.22	0.13	0.09	0.25	1.12	1.15
K_2O	2.75	2.21	1.99	1.52	2.49	1.50	1.77
P_2O_5	0.04	0.07	0.05	0.06	0.03	0.08	0.06
LOI	11.30	12.40	12.77	13.58	12.39	11.58	11.51
Total	100.55	100.46	100.88	100.75	100.49	100.63	101.07
CF%	19.5	21.8	18.9	35.5	34.3	37.8	36.3

LOI= Loss on ignition, CF%= Weight % of clay fraction in a sample

464

465

Table 2 Representative chemical compositions of Fe-kaolinite

Sample	M01	M01	M01	M01	M01	M07	M07	M07	M07	M07
No.	2	7	29	30	49	84	90	151	150	116
SiO_2 (wt.%)	43.69	44.50	44.05	44.47	43.71	47.44	44.82	49.93	48.30	46.19
TiO_2	0.24	0.06	0.00	0.00	0.00	0.09	0.02	0.00	0.40	0.06
Al_2O_3	31.97	33.75	34.22	34.07	35.18	31.93	31.38	36.59	33.04	35.24
Fe_2O_3	5.71	3.77	2.81	2.94	1.59	3.79	6.73	3.62	7.06	3.11
MnO	0.09	0.00	0.01	0.04	0.01	0.03	0.10	0.04	0.06	0.02
MgO	0.44	0.23	0.12	0.13	0.11	0.30	0.63	0.09	0.50	0.12
CaO	0.05	0.16	0.11	0.13	0.07	0.58	0.29	0.22	0.26	0.16
Na_2O	0.04	0.03	0.04	0.04	0.00	0.19	0.05	0.01	0.04	0.02
K_2O	1.25	0.48	0.24	0.25	0.24	1.29	1.95	0.17	1.84	0.40
Total	83.48	82.97	81.60	82.05	80.91	85.64	85.97	90.65	91.51	85.30
				Atoms per formula unit (apfu)						
Oxygen	7.000	7.000	7.000	7.000	7.000	7.000	7.000	7.000	7.000	7.000
Si	2.008	2.025	2.025	2.034	2.015	2.104	2.019	2.066	2.038	2.035
Ti	0.008	0.002	0.000	0.000	0.000	0.003	0.001	0.000	0.013	0.002
Al	1.732	1.810	1.854	1.837	1.912	1.669	1.666	1.785	1.643	1.830
Fe	0.198	0.129	0.097	0.101	0.055	0.127	0.228	0.113	0.224	0.103
Mn	0.004	0.000	0.000	0.001	0.000	0.001	0.004	0.001	0.002	0.001
Mg	0.030	0.016	0.008	0.009	0.007	0.020	0.043	0.006	0.032	0.008
Ca	0.002	0.008	0.005	0.006	0.003	0.028	0.014	0.010	0.012	0.008
Na	0.003	0.002	0.003	0.004	0.000	0.016	0.004	0.001	0.003	0.002
K	0.073	0.028	0.014	0.014	0.014	0.073	0.112	0.009	0.099	0.022
Total	4.058	4.019	4.008	4.006	4.008	4.040	4.091	3.990	4.066	4.009

This is a preprint, the final version is subject to change, of the American Mineralogist (MSA)
Cite as Authors (Year) Title. American Mineralogist, in press.
DOI: https://doi.org/10.2138/am-2018-6478

466

Table 3 Fitting results for Fe K-edge EXAFS of clay fractions

Sample	Shell	CN	R (Å)	ΔE_0 (eV)	σ^2 (Å^2)	R factor (%)
M01	Fe-O	4.2±1.0	1.97±0.02		0.08±0.03	
	Fe-Al	3.0 (fix)	2.94±0.06	-7	0.11±0.02	1.82
	Fe-Si	2.0 (fix)	3.24±0.01		0.04±0.05	
M07	Fe-O	4.7±1.0	1.97±0.02		0.09±0.03	
	Fe-Al	3.0 (fix)	2.95±0.07	-7.2	0.14±0.03	3.57
	Fe-Si	2.0 (fix)	3.29±0.02		0.08±0.04	

467

This is a preprint, the final version is subject to change, of the American Mineralogist (MSA)
Cite as Authors (Year) Title. American Mineralogist, in press.
DOI: https://doi.org/10.2138/am-2018-6478

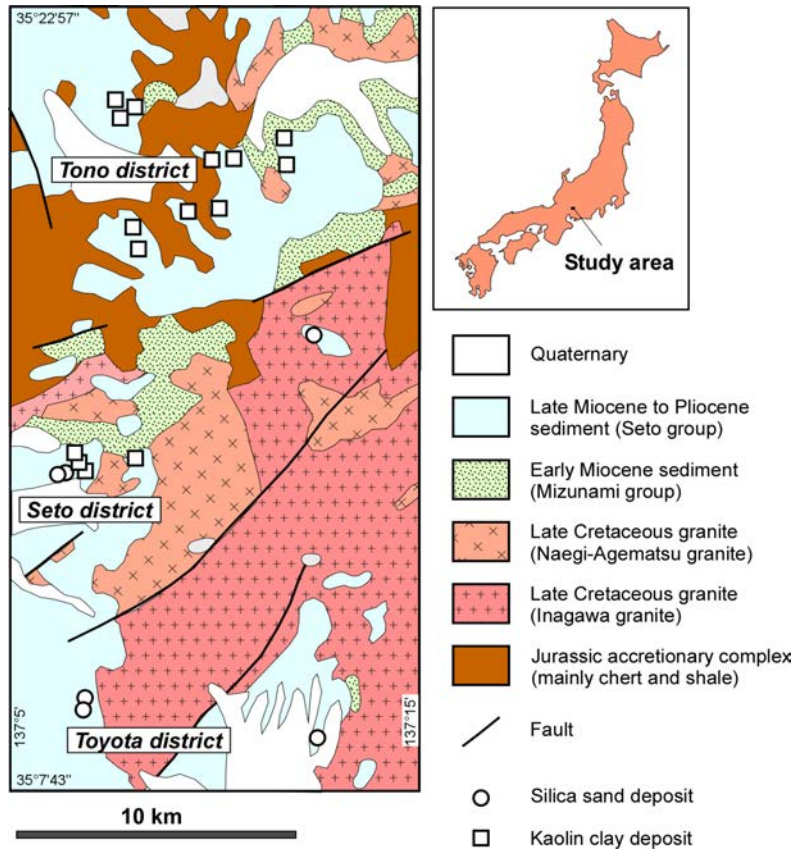

Fig. 1 Jige et al.

This is a preprint, the final version is subject to change, of the American Mineralogist (MSA)
Cite as Authors (Year) Title. American Mineralogist, in press.
DOI: https://doi.org/10.2138/am-2018-6478

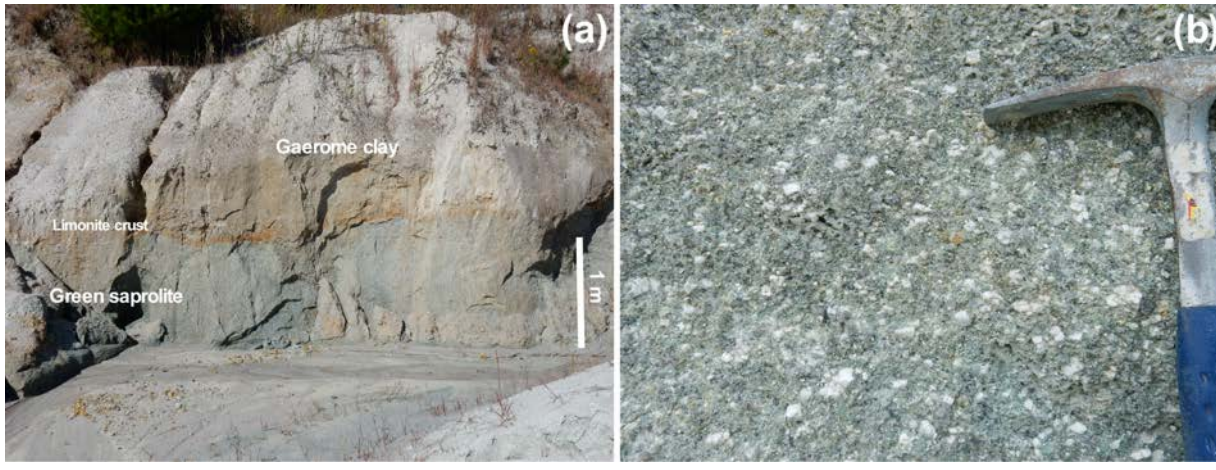

Fig. 2 Jige et al.

This is a preprint, the final version is subject to change, of the American Mineralogist (MSA)
Cite as Authors (Year) Title. American Mineralogist, in press.
DOI: https://doi.org/10.2138/am-2018-6478

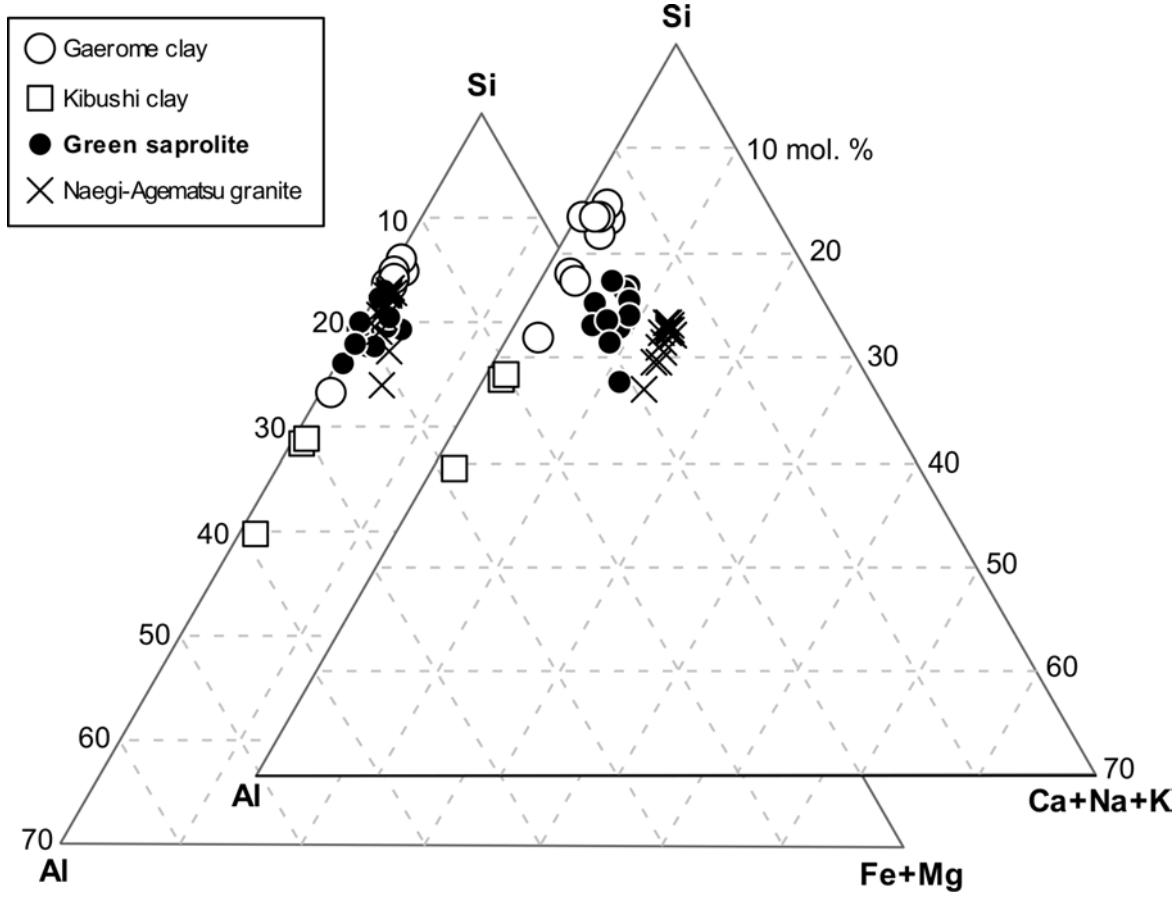

Fig. 3 Jige et al.

This is a preprint, the final version is subject to change, of the American Mineralogist (MSA)
Cite as Authors (Year) Title. American Mineralogist, in press.
DOI: https://doi.org/10.2138/am-2018-6478

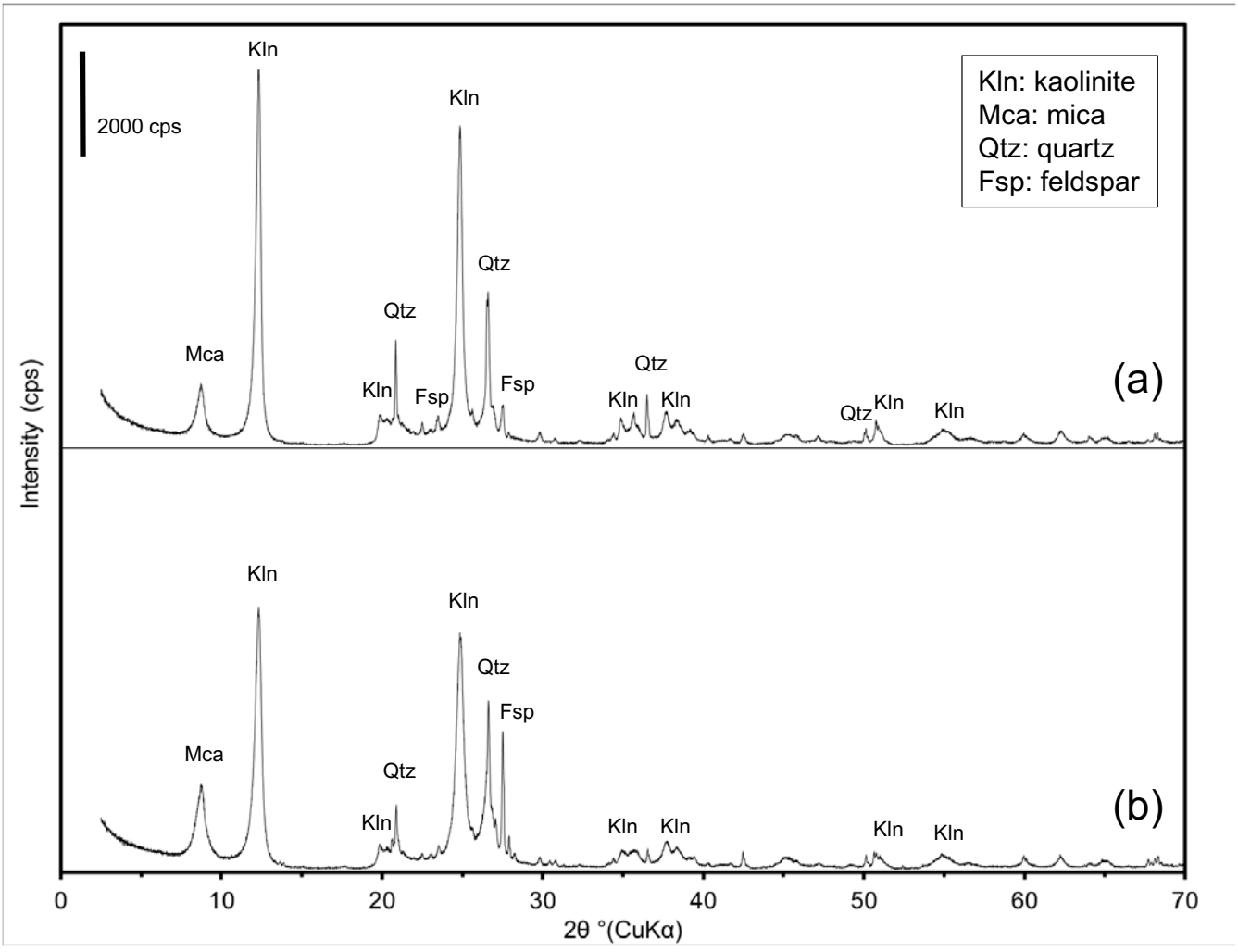

Fig. 4 Jige et al.

This is a preprint, the final version is subject to change, of the American Mineralogist (MSA)
Cite as Authors (Year) Title. American Mineralogist, in press.
DOI: https://doi.org/10.2138/am-2018-6478

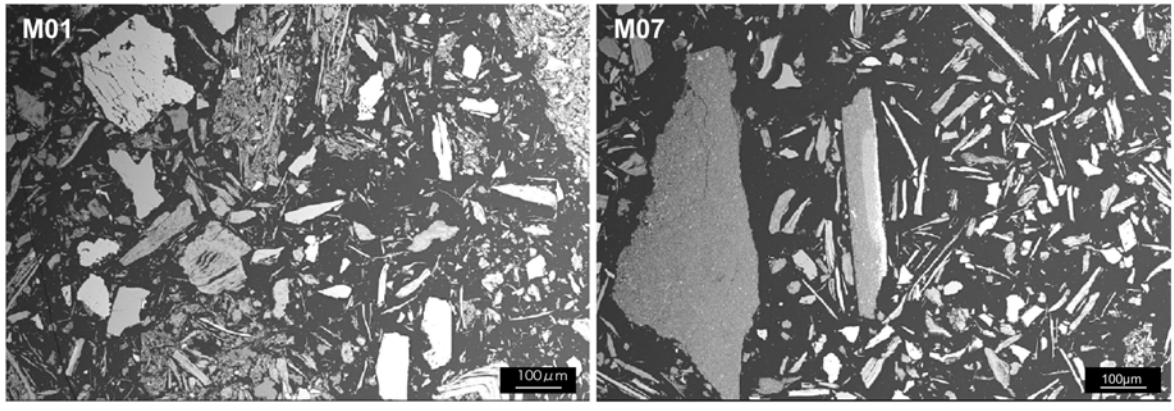

Fig. 5 Jige et al.

This is a preprint, the final version is subject to change, of the American Mineralogist (MSA)
Cite as Authors (Year) Title. American Mineralogist, in press.
DOI: https://doi.org/10.2138/am-2018-6478

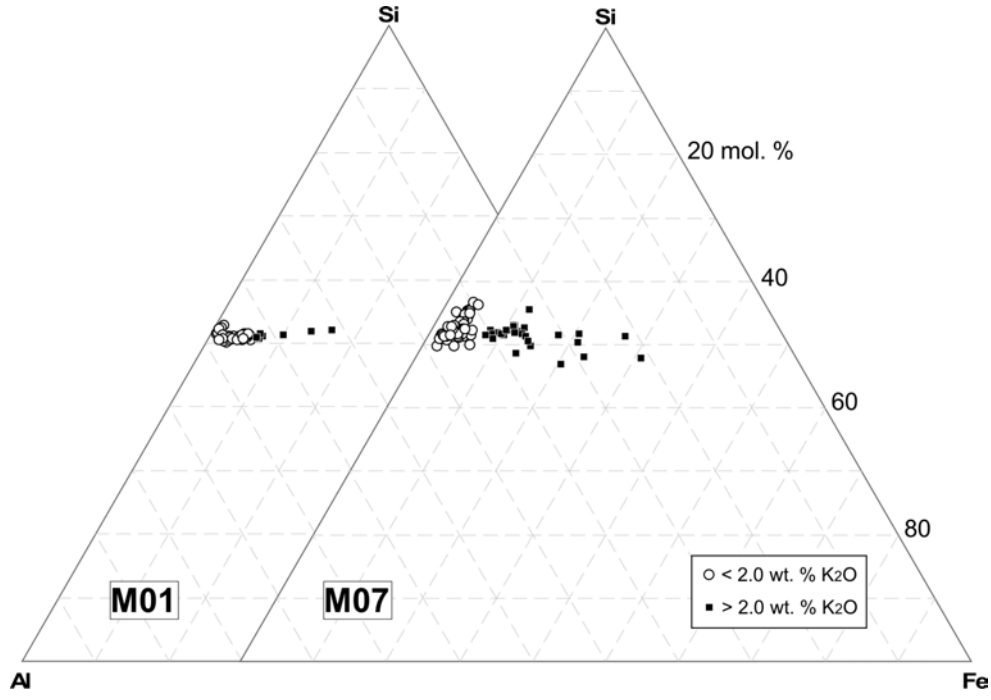

Fig. 6 Jige et al.

This is a preprint, the final version is subject to change, of the American Mineralogist (MSA)
Cite as Authors (Year) Title. American Mineralogist, in press.
DOI: https://doi.org/10.2138/am-2018-6478

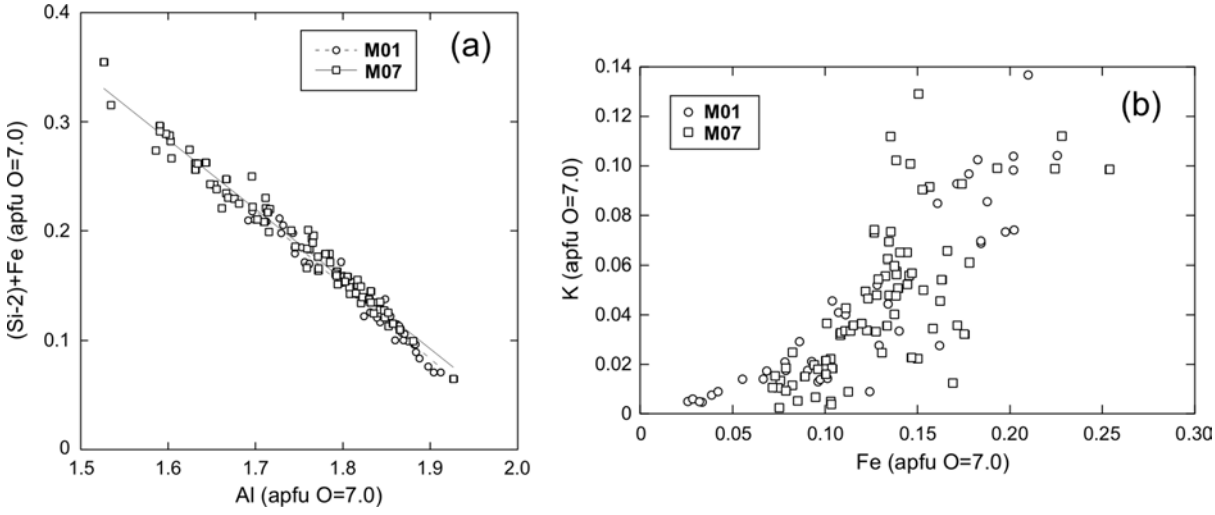

Fig. 7 Jige et al.

This is a preprint, the final version is subject to change, of the American Mineralogist (MSA)
Cite as Authors (Year) Title. American Mineralogist, in press.
DOI: https://doi.org/10.2138/am-2018-6478

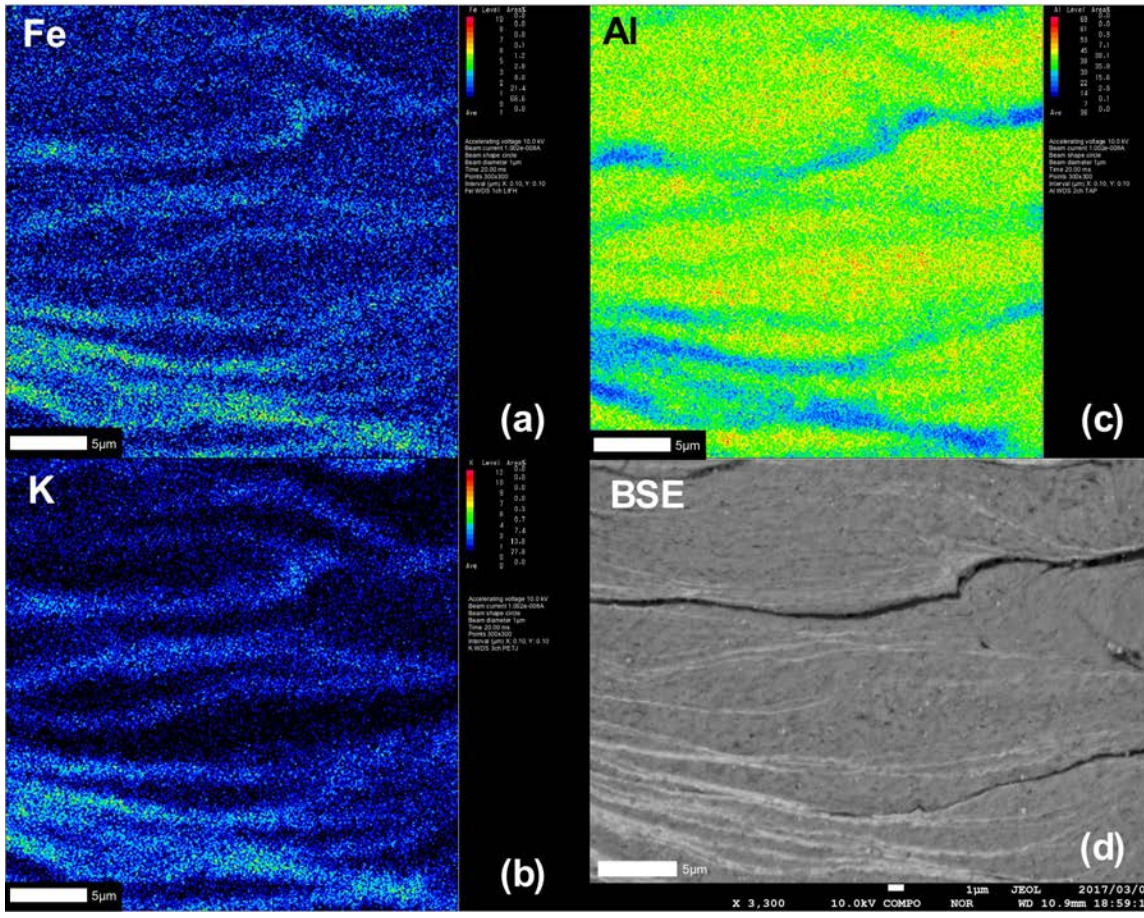

Fig. 8 Jige et al.

This is a preprint, the final version is subject to change, of the American Mineralogist (MSA)
Cite as Authors (Year) Title. American Mineralogist, in press.
DOI: https://doi.org/10.2138/am-2018-6478

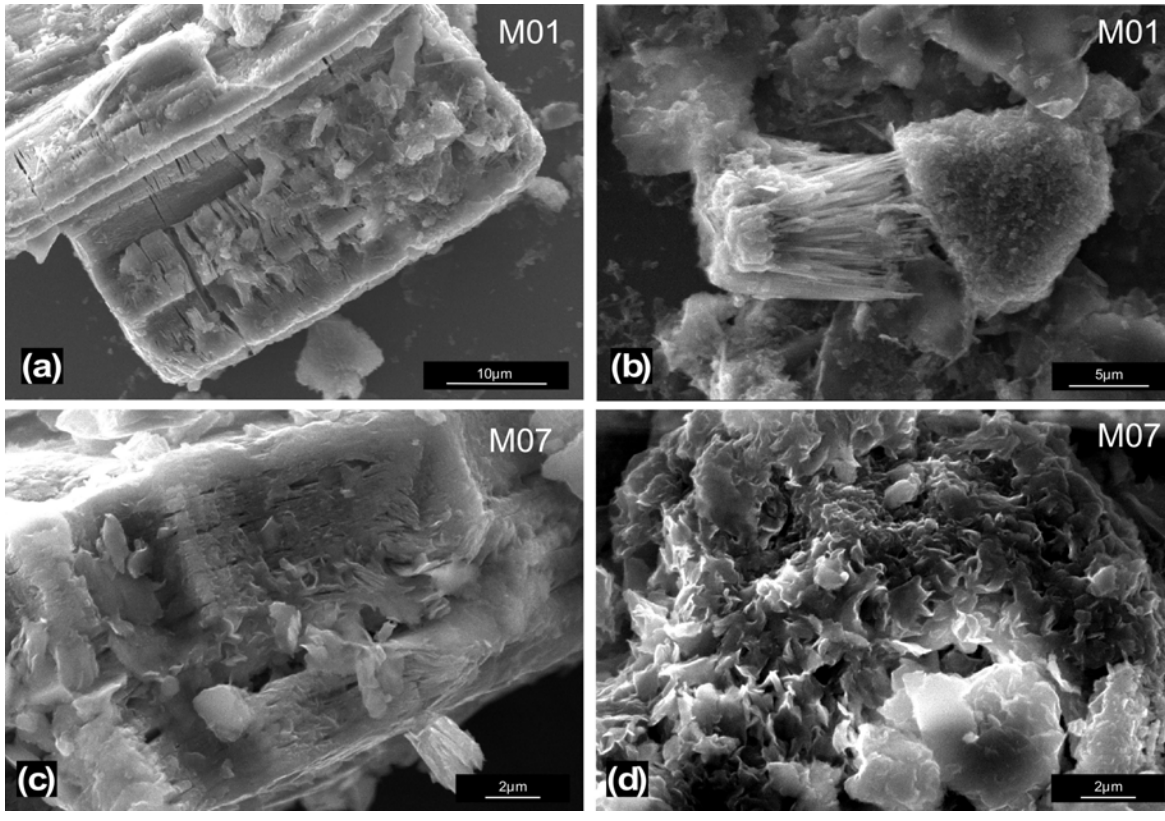

Fig. 9 Jige et al.

This is a preprint, the final version is subject to change, of the American Mineralogist (MSA)
Cite as Authors (Year) Title. American Mineralogist, in press.
DOI: https://doi.org/10.2138/am-2018-6478

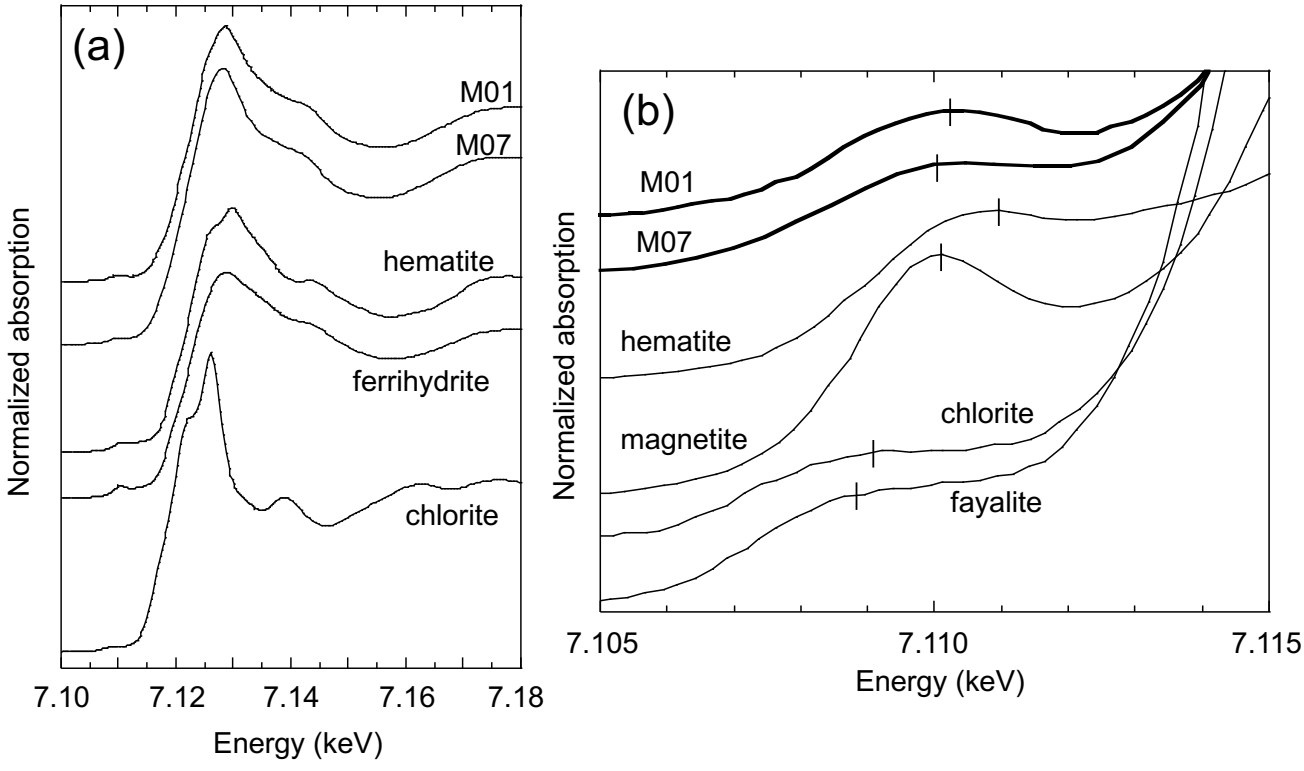

Fig. 10 Jige et al.

This is a preprint, the final version is subject to change, of the American Mineralogist (MSA)
Cite as Authors (Year) Title. American Mineralogist, in press.
DOI: https://doi.org/10.2138/am-2018-6478

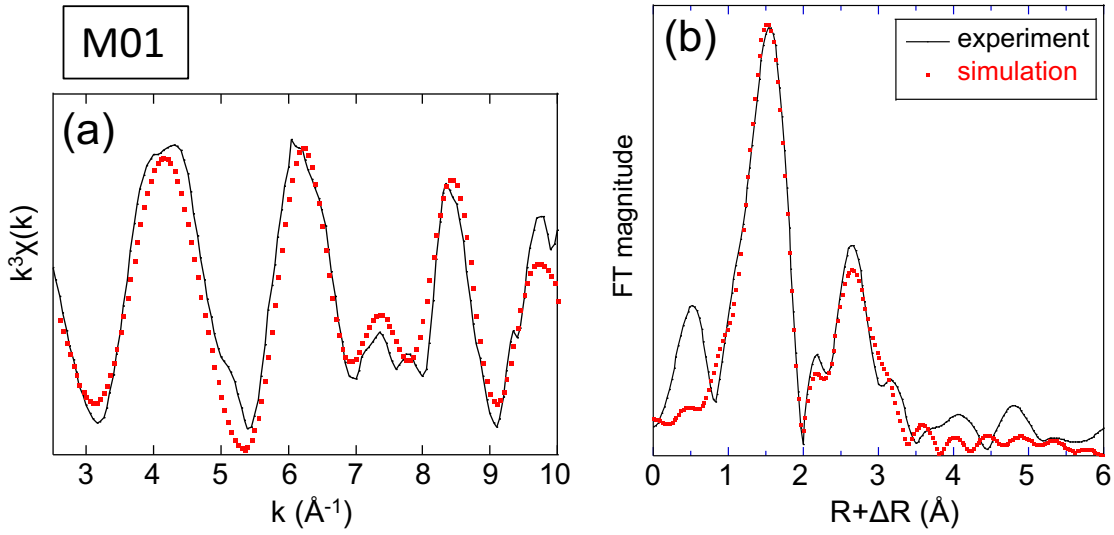

Fig. 11 Jige et al.

This is a preprint, the final version is subject to change, of the American Mineralogist (MSA)
Cite as Authors (Year) Title. American Mineralogist, in press.
DOI: https://doi.org/10.2138/am-2018-6478

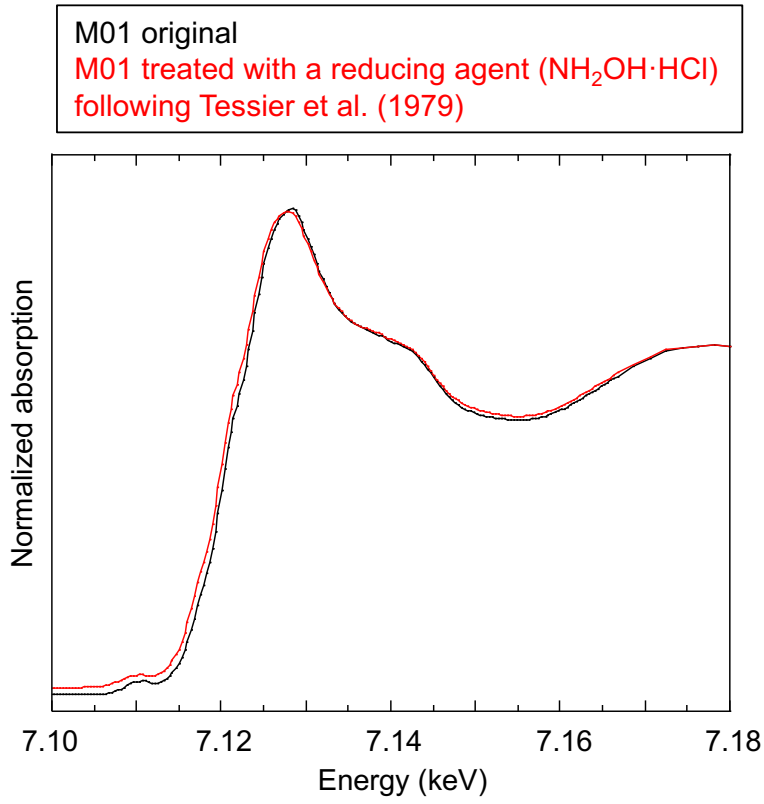

Fig. 12 Jige et al.

This is a preprint, the final version is subject to change, of the American Mineralogist (MSA)
Cite as Authors (Year) Title. American Mineralogist, in press.
DOI: https://doi.org/10.2138/am-2018-6478

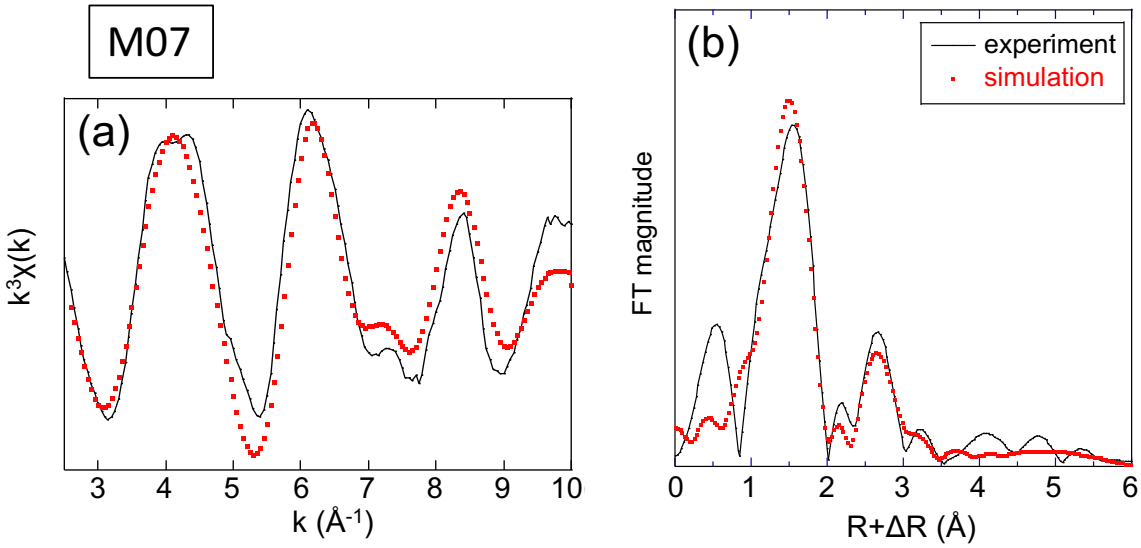

Fig. 13 Jige et al.

This is a preprint, the final version is subject to change, of the American Mineralogist (MSA)
Cite as Authors (Year) Title. American Mineralogist, in press.
DOI: https://doi.org/10.2138/am-2018-6478

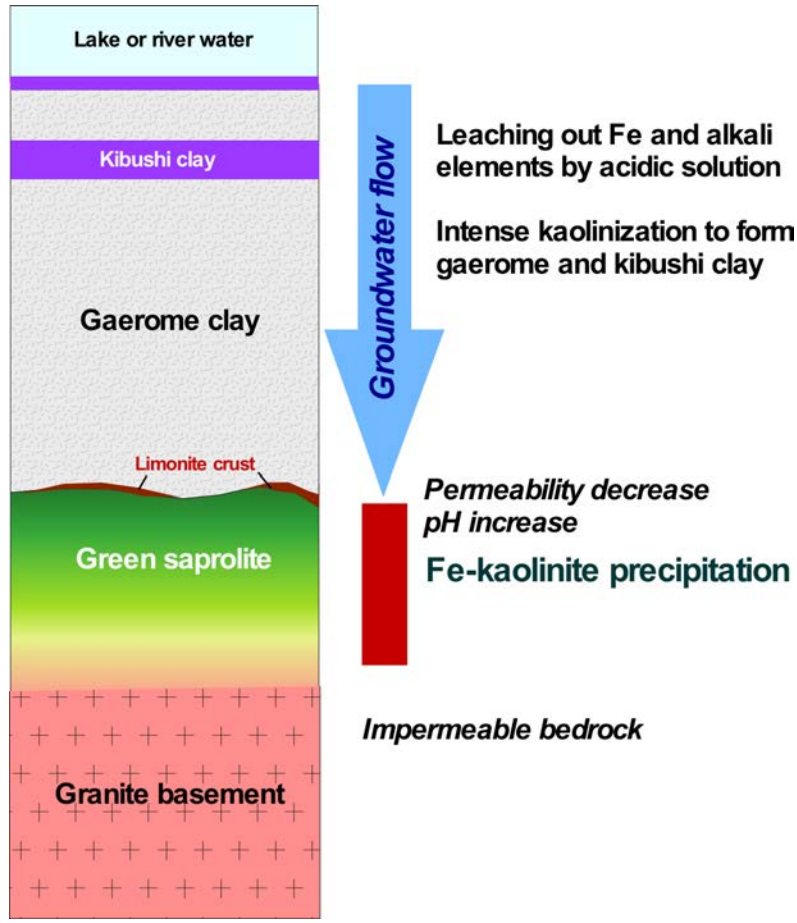

Fig. 14 Jige et al.

This is a preprint, the final version is subject to change, of the American Mineralogist (MSA)
Cite as Authors (Year) Title. American Mineralogist, in press.
DOI: https://doi.org/10.2138/am-2018-6478

Table 1 Chemical compositions of clay fractions in green saprolite

Sample	M01	M07	M08	M01a	M01b	M01c	M01d
SiO_2 (wt.%	51.58	49.59	49.10	48.15	50.93	50.21	51.02
TiO_2	0.63	0.55	0.76	0.97	0.45	0.48	0.45
Al_2O_3	29.92	29.45	32.92	34.12	30.99	30.83	30.24
Fe_2O_3	2.29	3.70	2.04	0.67	0.83	2.49	2.19
FeO	1.11	1.11	0.56	1.14	1.64	1.14	1.53
MnO	0.05	0.06	0.03	0.02	0.02	0.04	0.05
MgO	0.51	0.66	0.37	0.26	0.30	0.46	0.52
CaO	0.16	0.45	0.15	0.18	0.16	0.70	0.58
Na_2O	0.23	0.22	0.13	0.09	0.25	1.12	1.15
K_2O	2.75	2.21	1.99	1.52	2.49	1.50	1.77
P_2O_5	0.04	0.07	0.05	0.06	0.03	0.08	0.06
LOI	11.30	12.40	12.77	13.58	12.39	11.58	11.51
Total	100.55	100.46	100.88	100.75	100.49	100.63	101.07
CF%	19.5	21.8	18.9	35.5	34.3	37.8	36.3

LOI= Loss on ignition, CF%= Weight % of clay fraction in a sample

This is a preprint, the final version is subject to change, of the American Mineralogist (MSA)
Cite as Authors (Year) Title. American Mineralogist, in press.
DOI: https://doi.org/10.2138/am-2018-6478

Table 2 Representative chemical compositions of Fe-kaolinite

Sample	M01	M01	M01	M01	M01	M07	M07	M07	M07	M07
No.	2	7	29	30	49	84	90	151	150	116
SiO_2 (wt.%	43.69	44.50	44.05	44.47	43.71	47.44	44.82	49.93	48.30	46.19
TiO_2	0.24	0.06	0.00	0.00	0.00	0.09	0.02	0.00	0.40	0.06
Al_2O_3	31.97	33.75	34.22	34.07	35.18	31.93	31.38	36.59	33.04	35.24
Fe_2O_3	5.71	3.77	2.81	2.94	1.59	3.79	6.73	3.62	7.06	3.11
MnO	0.09	0.00	0.01	0.04	0.01	0.03	0.10	0.04	0.06	0.02
MgO	0.44	0.23	0.12	0.13	0.11	0.30	0.63	0.09	0.50	0.12
CaO	0.05	0.16	0.11	0.13	0.07	0.58	0.29	0.22	0.26	0.16
Na_2O	0.04	0.03	0.04	0.04	0.00	0.19	0.05	0.01	0.04	0.02
K_2O	1.25	0.48	0.24	0.25	0.24	1.29	1.95	0.17	1.84	0.40
Total	83.48	82.97	81.60	82.05	80.91	85.64	85.97	90.65	91.51	85.30
					Atoms per formula unit (apfu)					
Oxygen	7.000	7.000	7.000	7.000	7.000	7.000	7.000	7.000	7.000	7.000
Si	2.008	2.025	2.025	2.034	2.015	2.104	2.019	2.066	2.038	2.035
Ti	0.008	0.002	0.000	0.000	0.000	0.003	0.001	0.000	0.013	0.002
Al	1.732	1.810	1.854	1.837	1.912	1.669	1.666	1.785	1.643	1.830
Fe	0.198	0.129	0.097	0.101	0.055	0.127	0.228	0.113	0.224	0.103
Mn	0.004	0.000	0.000	0.001	0.000	0.001	0.004	0.001	0.002	0.001
Mg	0.030	0.016	0.008	0.009	0.007	0.020	0.043	0.006	0.032	0.008
Ca	0.002	0.008	0.005	0.006	0.003	0.028	0.014	0.010	0.012	0.008
Na	0.003	0.002	0.003	0.004	0.000	0.016	0.004	0.001	0.003	0.002
K	0.073	0.028	0.014	0.014	0.014	0.073	0.112	0.009	0.099	0.022
Total	4.058	4.019	4.008	4.006	4.008	4.040	4.091	3.990	4.066	4.009

This is a preprint, the final version is subject to change, of the American Mineralogist (MSA)
Cite as Authors (Year) Title. American Mineralogist, in press.
DOI: https://doi.org/10.2138/am-2018-6478

Table 3 Fitting results for Fe K-edge EXAFS of clay fractions

Sample	Shell	CN	R (Å)	ΔE_0 (eV)	σ^2 (Å^2)	R factor (%)
M01	Fe-O	4.2±1.0	1.97±0.02		0.08±0.03	
	Fe-Al	3.0 (fix)	2.94±0.06	-7	0.11±0.02	1.82
	Fe-Si	2.0 (fix)	3.24±0.01		0.04±0.05	
M07	Fe-O	4.7±1.0	1.97±0.02		0.09±0.03	
	Fe-Al	3.0 (fix)	2.95±0.07	-7.2	0.14±0.03	3.57
	Fe-Si	2.0 (fix)	3.29±0.02		0.08±0.04	